Numerical analysis of a solar tower receiver tube operated with liquid metals

L. Marocco [a, b, *], G. Cammi [b], J. Flesch [a], Th. Wetzel [a]

[a] Karlsruhe Institute of Technology (KIT), Institute for Nuclear and Energy Technologies, Hermann-von-Helmholtz-Platz 1, 76344 Eggenstein-Leopoldshafen, Germany
[b] Politecnico di Milano, Department of Energy, via Lambruschini 4, 20156 Milan, Italy

Computational fluid dynamics is used in the present work to analyze the conjugate heat transfer in the receiver tube of a solar thermal tower operated with a liquid metal. A circumferentially and longitudi-nally non-uniform heat flux, due to solar irradiation, is applied on half the external surface while the other one is considered as insulated. The heat transfer mechanism of liquid metals differs from that of ordinary fluids. As a consequence, the Reynolds analogy, which assumes a constant turbulent Prandtl number close to unity, cannot be applied to these fluid flows. Therefore two additional equations, namely one for the temperature variance and one for its dissipation rate are additionally solved, in order to determine the turbulent thermal diffusivity. The effects of the wall thickness ratio, the solid-to-fluid thermal conductivity ratio, the Péclet number and the diameter-to-length ratio have been analyzed.

The calculated average Nusselt numbers closely agree with those evaluated with appropriate corre-lations for liquid metals, valid for uniformly distributed heat flux. Nonetheless these are not suited to evaluate the local Nusselt number and wall temperature distribution.

Keywords: Liquid metals, CFD, Turbulent convection Pipe flow, Solar receiver

1. Introduction

Liquid metals are considered as efficient heat transfer media in many processes with exceptionally high thermal loads. They have been already proposed in the past as high temperature heat transfer media in concentrating solar power systems. Indeed, during the 80s, tests have been carried out on a demonstration plant (Plataforma Solar de Almeria) operated with a liquid sodium-cooled central receiver [1,2]. Unfortunately, the experiments have been stopped after a fire, caused by a sodium leakage during improper maintenance work. Recently, after a period of reduced interest in that approach, several new efforts have been reported, such as thermodynamic evaluation of candidate liquid alloys [3], as well as corrosion and heat transfer tests [4]. Further works, as e.g. those reported in Refs. [5–10] have recently highlighted the attractive properties of liquid metals for Concentrated Solar Power (CSP) applications. Presently a small concentrating solar power system operated with lead-bismuth eutectic ($Pr = 0.025$) is under construction at the Karlsruhe Institute of Technology in Germany, as discussed in Ref. [11].

In a solar tower plant, a field of sun-tracking mirrors, called heliostats, concentrate the sunlight onto a tower-mounted, centrally located receiver. The incident solar energy heats a fluid which, in case of a liquid metal, subsequently transfers its energy to the operating fluid of the power cycle. Compared to other technologies such as parabolic through, Fresnel and dish collectors, solar tower thermal plants are expected to reach lower levelized electricity costs [12,13]. The central receiver is a key component and accounts for about 15% of the total investment costs [14]. One typical arrangement for the receiver is based on arrays of parallel tubes, which are cooled from the inside by a heat transfer fluid and heated from the outside by the concentrated sunlight. In this design, only half of the tubes' surface is exposed to solar irradiance, resulting in a strongly non-uniform heat flux on the outer wall. This can result in high thermal stresses in the tube walls, whose magnitude depends on the cooling effect of the heat transfer fluid. Thus, for a proper thermo-hydraulic, as well as mechanical design of the receiver, good knowledge of the local wall temperatures and convective heat transfer coefficients is required.

Liquid metals are characterized by a high molecular thermal

Article history:
Received 11 March 2015
Received in revised form
29 January 2016
Accepted 9 February 2016
Available online 10 March 2016

* Corresponding author. Karlsruhe Institute of Technology (KIT), Institute for Nuclear and Energy Technologies, Hermann-von-Helmholtz-Platz 1, 76344 Eggenstein-Leopoldshafen, Germany; Politecnico di Milano, Department of Energy, via Lambruschini 4, 20156 Milan, Italy.
E-mail addresses: luca.marocco@kit.edu, luca.marocco@polimi.it (L. Marocco).

Published Journal Article available at: http://dx.doi.org/10.1016/j.ijthermalsci.2016.02.002

Nomenclature

Roman letters

C_f	Fanning friction factor $(-)$
c_p	specific heat capacity at constant pressure (J/kgK)
C_μ, $C_{1\varepsilon}$, $C_{2\varepsilon}$	constants in momentum turbulence model, Table 1 $(-)$
C_θ, C_{d1}, C_{p1}, C_{p2}, $Pr_{t\infty}$	constants in heat turbulence model, Table 2 $(-)$
C_{d2}	function in heat turbulence model, Eq. (32) $(-)$
D	internal diameter $D = 2r_i$ (m)
$f_{1\mu}$,$f_{2\mu}$,f_ε	functions in momentum turbulence model, Eqs. (16)–(18) $(-)$
$f_{1\theta}$, $f_{2\theta}$, $f_{2a\theta}$, $f_{2b\theta}$	functions in heat turbulence model, Eqs. (27) – (30) $(-)$
Gr	Grashof number $Gr = g\beta q'' D^4/(\lambda\nu^2)$ $(-)$
$\boldsymbol{I}$	identity vector $(-)$
k	turbulent kinetic energy (m^2/s^3)
k_θ	variance of temperature fluctuations, Eq. (9) (K^2)
L	tube's length (m)
Nu	Nusselt number $(-)$
P	average static pressure (Pa)
P_θ	production term in heat turbulence model, Eq. (25) (K^2/s)
P_k	turbulent kinetic energy production, Eq. (14) (m^2/s^3)
Pe	Péclet number $Pe = RePr$ $(-)$
Pr	Prandtl number $(-)$
Pr_t	turbulent Prandtl number $Pr_t = \nu_t/\alpha_t$
$\tilde{q}''_w$	non-dimensional wall heat flux $(-)$
q''	heat flux (W/m^2)
R	ratio between thermal and dynamical characteristic time $R = \tau_\theta/\tau_u$, Eq. (31) $(-)$
R_δ	Kolmogorov Reynolds number, Eq. (20) $(-)$
R_t	turbulent Reynolds number, Eq. (19) $(-)$
Re	Reynolds number $Re = u_b D/\nu$ $(-)$
Ri	Richardson number $Ri = Gr/Re^2$ $(-)$
r	tube radius (m)
r^*	outer-to-inner radius ratio $r^* = r_o/r_i$ non-dimensional radial coordinate $r^* = r/r_i$ $(-)$
r^+	non-dimensional wall distance $r^+ = u_\tau r/\nu$ $(-)$
$\boldsymbol{S}$	mean strain rate tensor (s^{-1})
T	temperature (K)
T'	temperature fluctuations (K)
T^+	non-dimensional temperature $T^+ = (T_w - T)/T_\tau$ $(-)$
T_τ	friction temperature $T_\tau = q''/\rho u_\tau c_p$ (K)
T_{b0}	inlet bulk temperature (K)
t	time (s)
$\boldsymbol{u}$	velocity vector (m/s)
$\boldsymbol{u}'$	vector of mean velocity fluctuations (m/s)
u'_r	fluctuating radial velocity (m/s)
$\overline{\boldsymbol{u}'T'}$	turbulent heat flux vector (mK/s)
u_τ	friction velocity $u_\tau = (\tau_w/\rho)^{0.5}$ (m/s)
$\overline{u'_r T'}^+$	non-dimensional radial turbulent heat flux $\frac{\overline{u'_r T'}}{u_\tau T_\tau}$ $(-)$
$\overline{\boldsymbol{u}' \otimes \boldsymbol{u}'}$	Reynolds stress tensor (m^2/s^2)
Δx	dimensional axial mesh spacing (m)
Δx^+	non-dimensional axial mesh spacing $\Delta x^+ = u_\tau \Delta x/\nu$ $(-)$
$\tilde{x}$	non-dimensional axial coordinate $\tilde{x} = x/L$ $(-)$
y^+	non-dimensional wall distance $y^+ = u_\tau \delta/\nu$ $(-)$

Greek letters

α	molecular thermal diffusivity (m^2/s)
α_t	turbulent thermal diffusivity (m^2/s)
δ	distance from the wall (m)
ε	turbulent kinetic energy dissipation rate (m^2/s^3)
ε_θ	dissipation rate of temperature fluctuations, Eq. (9) (K^2/s)
θ_{iw}, θ_{ow}, θ_b	dimensionless inner Eq. (38), outer Eq. (39) and bulk Eq. (40) temperature
λ	molecular thermal conductivity (W/mK)
λ^*	solid-to-fluid thermal conductivity ratio $\lambda^* = \lambda_s/\lambda_f$
ν	kinematic viscosity (m^2/s)
ν_t	turbulent kinematic viscosity (m^2/s)
ρ	density (kg/m^3)
σ_k, σ_ε	constants in momentum turbulence model, Table 1
$\sigma_{k\theta}$, $\sigma_{\varepsilon\theta}$	constants in heat turbulence model, Table 2
τ_w	wall shear stress (N/m^2)
$\tau_{l\theta}$	local thermal characteristic time, Eq. (26) (s)
τ_{lu}	local dynamical characteristic time, Eq. (15) (s)
τ_θ	thermal turbulent characteristic time $\tau_\theta = k_\theta/\varepsilon_\theta$ (s)
τ_u	dynamical turbulent characteristic time $\tau_u = k/\varepsilon$ (s)

Operators

$\overline{(\bullet)}$	Reynolds-averaged values
$\langle\bullet\rangle$	circumferentially averaged value cross-section averaged
$\langle\bullet\rangle_L$	circumferentially and longitudinally averaged value
$(\bullet)$	scalar product
∇	gradient
$(\bullet)^T$	transposed matrix
$(\bullet)\|_w$	value at the wall
$\otimes$	outer product

Subscripts

b	bulk
f	fluid
fd	fully developed
i	inner
o	outer
s	solid
iw	inner wall
ow	outer wall

conductivity and a low Prandtl number. This results in a heat transfer mechanism different from that of fluids with medium-to-high Pr numbers. Indeed, the thickness of the thermal viscous sublayer is considerably greater than that of the hydrodynamic viscous sublayer [15]. As a consequence, neither the Reynolds analogy [16], which assumes a constant turbulent Prandtl number close to unity, nor the well established Gnielinski or Dittus–Boelter correlations [17] can be applied to liquid metal flows. A recent review of the available Nusselt number correlations appropriate for fully developed forced convection to liquid metal flows in tubes can be found in Ref. [18]. Moreover, the above mentioned circumferentially non-uniform heat flux distribution of the concentrated sunlight creates some doubt about the applicability of correlations developed for uniformly heated tubes.

In the present work the computational fluid dynamics (CFD) code FLUENT v.15 has been used to analyze the turbulent convective flow of a representative liquid metal inside a solar tower receiver tube subject to circumferentially and longitudinally non-uniform heat flux conditions on the outer wall surface, as shown in Fig. 1.

Presently, according to the authors' knowledge, there are no investigations for liquid metal flows subject to these boundary conditions. On the contrary there are some experimental and numerical works for steam [19], water [20], two-phase water-steam mixture [21] and molten salts [22,23]. Also the papers of [24] and [25] are worth mentioning. Here the problem of a hydrodynamically and thermally fully developed flow in a tube with a circumferentially periodic boundary condition, e.g. a sinusoidal heat flux distribution over the entire tube's wall, has been analytically solved, in principle for all Pr numbers. Actually their approach is limited by the assumptions made to evaluate the turbulent Prandtl number, Pr_t.

A recently proposed turbulence model by Manservisi and Menghini [26] to directly compute the turbulent thermal diffusivity of heat, α_t, in low-Pr number fluids has therefore been used in this work. This necessitates the solution of two additional transport equations, namely one for the temperature variance, k_θ, and one for its dissipation, ε_θ. These are not already implemented in the standard version of FLUENT v.15 and have been therefore separately coded and coupled to the software through user-defined-functions (UDF). In view of the considerations in Refs. [9,11], a fluid having $Pr = 0.025$ has been chosen, encompassing mercury, gallium-indium-tin and especially lead-bismuth eutectic. Please note that the first two are not considered for CSP applications but might be used as model fluids for thermo-hydraulic experiments.

2. Governing equations

The numerical simulations have been performed for a steady flow neglecting buoyancy forces, viscous dissipation and considering constant thermo-physical properties. The results refer then to sufficiently low Richardson numbers, $Ri = Gr/Re^2$, such that natural convection effects could be actually neglected. The time-averaged governing equations for mass, momentum and energy can be written as:

$$\nabla\cdot\boldsymbol{u} = 0 \tag{1}$$

$$\boldsymbol{u}\cdot\nabla\boldsymbol{u} = \nabla\cdot\left(2\nu\boldsymbol{S} - \overline{\boldsymbol{u}'\otimes\boldsymbol{u}'}\right) - \frac{1}{\rho}\nabla P \tag{2}$$

$$\boldsymbol{u}\cdot\nabla T = \nabla\cdot\left(\alpha\nabla T - \overline{\boldsymbol{u}'T'}\right) \tag{3}$$

In the above equations, the mean strain rate tensor is defined as $\boldsymbol{S}: = 0.5(\nabla\boldsymbol{u}+\nabla\boldsymbol{u}^T)$, while for the unknown Reynolds stress tensor, $\overline{\boldsymbol{u}'\otimes\boldsymbol{u}'}$, and turbulent heat flux vector, $\overline{\boldsymbol{u}'T'}$, appropriate evolution equations should be written for each of their components. Instead, Algebraic Stress Models (ASM) for Reynolds stresses and Algebraic Flux Models (AHF) for turbulent heat fluxes can be used. These are deduced by starting from the corresponding full second order transport equations and assuming the so called *weak non-equilibrium hypothesis*, by which the time and space evolution of the stress anisotropy tensor and of the turbulent thermal flux is approximately zero. This results in implicit algebraic expressions for $\overline{\boldsymbol{u}'\otimes\boldsymbol{u}'}$ and $\overline{\boldsymbol{u}'T'}$. For the former the remaining closure terms are modeled with expressions containing the turbulent kinetic energy, k, and its dissipation rate, ε, so that the resulting number of additional equations is 2. For the latter, considering buoyant flows and Prandtl numbers different from unity, apart from k and ε also the temperature variance, Eq. (21), and its dissipation rate, Eq. (22), are needed, so that the equations become 2+2. Algebraic models could be attractive for flows with strong anisotropic momentum and heat exchange and counter-gradient momentum and heat fluxes. Nevertheless their intrinsic implicit character could lead to numerical problems. Examples of these approaches, partially adapted also to low Prandtl number fluids, can be found in the following references [27–29].

The closure problem can be further simplified by using the Boussinesq assumption of a turbulent diffusivity of momentum and heat (Single Gradient Diffusion Hypothesis) so that $\overline{\boldsymbol{u}'\otimes\boldsymbol{u}'}$ and $\overline{\boldsymbol{u}'T'}$ can be written as follows:

$$\overline{\boldsymbol{u}'\otimes\boldsymbol{u}'} = -2\nu_t\boldsymbol{S} + \frac{2}{3}k\boldsymbol{I} \tag{4}$$

$$\overline{\boldsymbol{u}'T'} = -\alpha_t\nabla T \tag{5}$$

The turbulent thermal diffusivity in Eq. (5) can be expressed in terms of the turbulent momentum diffusivity by defining a turbulent Prandtl number:

$$Pr_t = \frac{\nu_t}{\alpha_t} \tag{6}$$

In engineering practice the turbulent viscosity is calculated by solving appropriate evolution equations for some quantities used to characterize the time and length scale of turbulence, but the turbulent Prandtl number is typically specified as a constant value. While this hypothesis, also known as *Reynolds analogy*, may be

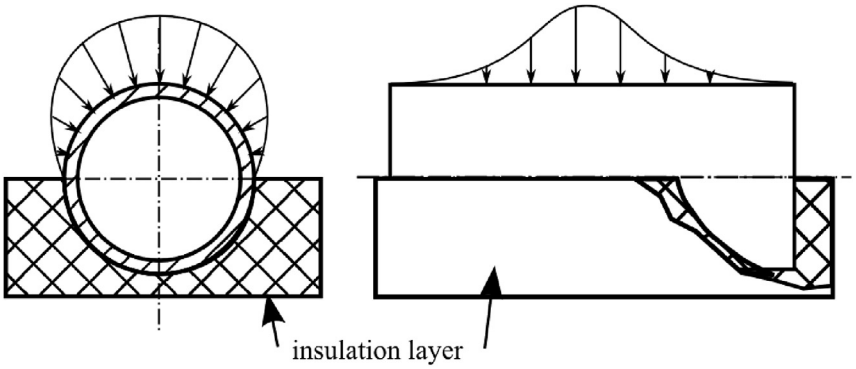

Fig. 1. Non-uniform thermal boundary conditions for the CFD simulations.

approximately valid for medium-to-high Prandtl number fluids, it cannot be applied to low-Pr number fluids as e.g. shown by the direct numerical simulations (DNS) in a channel flow [30–33], or in the work presented in Refs. [34–36], where it fails to reproduce the available heat transfer correlations in various geometries. The main reason is the very high thermal conductivity of liquid metals, which causes the instantaneous temperature field to be much smoother than the velocity field [37]. Indeed, the smallest temperature scales are much larger than the respective velocity scales. The conductive viscous sublayer is thus thicker than the hydrodynamic one, so that the conductive heat flux plays a prominent role in the heat transfer process [38]. Some correlations for Pr_t have been proposed, but independently of whether they depend on global parameters, like the flow Reynolds number, or local ones, like ν_t, their validity is mostly restricted to the geometries they have been developed for. A good overview of several correlations and their assessment to liquid metal flows can be found in Refs. [35–37].

3. $k-\varepsilon-k_\theta-\varepsilon_\theta$ turbulence model

Recently, a four-equation turbulence model considering the thermal turbulence effects and the dissimilarities between the thermal and dynamical turbulence fields has been proposed in Ref. [26]. Here, ν_t is expressed as follows:

$$\nu_t = C_\mu k \tau_{lu} \tag{7}$$

where the local dynamical characteristic time of turbulence, τ_{lu}, is determined from the solution of a transport equation for the turbulent kinetic energy, k, and one for its dissipation rate ε.

The turbulent thermal diffusivity α_t, and thus the turbulent Prandtl number, is expressed as follows:

$$\alpha_t = C_\theta k \tau_{l\theta} \tag{8}$$

where the local thermal characteristic time of turbulence, $\tau_{l\theta}$, is evaluated from the above mentioned k and ε fields and from the solution of two additional equations, namely one for the variance of the temperature fluctuations, k_θ, and one for its dissipation rate, ε_θ:

$$k_\theta = \frac{1}{2}\overline{T'^2}, \quad \varepsilon_\theta = \frac{\nu}{Pr}\overline{\left|\nabla T'\right|^2} \tag{9}$$

For a thorough description of the model and its derivation, the interested reader is referred to [26,36] and references therein.

In the following paragraphs the steady-state equations for the momentum and heat turbulence for an incompressible newtonian fluid are reported, together with their corresponding constants, damping functions and definition of the various parameters.

3.1. Momentum turbulence equations

The formulation for the turbulent $k-\varepsilon$ model used, and listed in what follows, is the same as the one proposed by Abe et al. [39] and will be denoted as AKN.

$$\boldsymbol{u}\cdot\nabla k = \nabla\cdot\left[\left(\nu+\frac{\nu_t}{\sigma_k}\right)\nabla k\right] + P_k - \varepsilon \tag{10}$$

$$\boldsymbol{u}\cdot\nabla \varepsilon = \nabla\cdot\left[\left(\nu+\frac{\nu_t}{\sigma_\varepsilon}\right)\nabla \varepsilon\right] + C_{1\varepsilon}\frac{\varepsilon}{k}P_k - C_{2\varepsilon}\frac{\varepsilon^2}{k}f_\varepsilon \tag{11}$$

The following boundary conditions apply at the walls:

$$\left.\frac{dk}{d\delta}\right|_\omega = \frac{2k}{\delta} \tag{12}$$

$$\varepsilon|_\omega = \nu\frac{2k}{\delta^2} \tag{13}$$

The production of turbulent kinetic energy, P_k, in Eqs. (10) and (11) and the local dynamical characteristic time of turbulence in Eq. (7) are expressed as:

$$P_k = \frac{\nu_t}{2}\left|\nabla\boldsymbol{u} + \nabla\boldsymbol{u}^T\right|^2 \tag{14}$$

$$\tau_{lu} = \frac{k}{\varepsilon}\left(f_{1\mu} + f_{2\mu}\frac{5}{R_t^{3/4}}\right) \tag{15}$$

The definitions for the different parameters and damping functions are listed below:

$$f_{1\mu} = (1-\exp(-0.0714R_\delta))^2 \tag{16}$$

$$f_{2\mu} = f_{1\mu}\exp\left(-2.5\times10^{-5}R_t^2\right) \tag{17}$$

$$f_\varepsilon = (1-\exp(-0.3226R_\delta))^2\left(1-0.3\exp(-0.0237R_t^2\right) \tag{18}$$

$$R_t = \frac{k^2}{\nu\varepsilon} \tag{19}$$

$$R_\delta = \frac{\delta(\varepsilon\nu)^{1/4}}{\nu} \tag{20}$$

In Eq. (20), δ is the distance from the wall. The constants appearing in Eq. (7) and in Eqs. (10) – (20) are listed in Table 1.

3.2. Heat turbulence equations

$$\boldsymbol{u}\cdot\nabla k_\theta = \nabla\cdot\left[\left(\alpha+\frac{\alpha_t}{\sigma_{k\theta}}\right)\nabla k_\theta\right] + P_\theta - \varepsilon_\theta \tag{21}$$

$$\boldsymbol{u}\cdot\nabla \varepsilon_\theta = \nabla\cdot\left[\left(\alpha+\frac{\alpha_t}{\sigma_{\varepsilon\theta}}\right)\nabla \varepsilon_\theta\right] + \frac{\varepsilon_\theta}{k_\theta}\left(C_{p1}P_\theta - C_{d1}\varepsilon_\theta\right) + \frac{\varepsilon_\theta}{k}\left(C_{p2}P_k - C_{d2}\varepsilon\right) \tag{22}$$

The following boundary conditions apply at the walls:

$$k_\theta|_\omega = 0 \tag{23}$$

$$\varepsilon_\theta|_\omega = \alpha\frac{2k_\theta}{\delta^2} \tag{24}$$

The production term, P_θ, in Eqs. (21) and (22) and the local thermal characteristic time of turbulence in Eq. (8) are expressed as:

Table 1
Constants for the momentum turbulence model.

C_μ	σ_k	σ_ε	$C_{1\varepsilon}$	$C_{2\varepsilon}$
0.09	1.4	1.4	1.5	1.9

Table 2
Constants for the heat turbulence model.

C_θ	$\sigma_{k\theta}$	$\sigma_{\varepsilon\theta}$	C_{p1}	C_{d1}	C_{p2}	$Pr_{t\infty}$	C_γ
0.1	1.4	1.4	0.925	1.0	0.9	0.9	0.3

$$P_\theta = \alpha_t \left|\nabla T\right|^2 \tag{25}$$

$$\tau_{l\theta} = \frac{k}{\varepsilon}(f_{1\theta} Pr_{t\infty} + f_{2\theta}) \tag{26}$$

The definitions for the different parameters and damping functions are listed below:

$$f_{1\theta} = Big(1 - \exp(-0.0526\sqrt{Pr}R_\delta)Big)(1 - \exp(-0.0714R_\delta) \tag{27}$$

$$f_{2\theta} = f_{2a\theta}\frac{2R}{R + C_\gamma} + f_{2b\theta}\sqrt{\frac{2R}{Pr}}\,\frac{1.3}{\sqrt{Pr}R_t^{3/4}} \tag{28}$$

$$f_{2a\theta} = f_{1\theta}\exp\left(-4 \times 10^{-6} R_t^2\right) \tag{29}$$

$$f_{2b\theta} = f_{1\theta}\exp\left(-2.5 \times 10^{-5} R_t^2\right) \tag{30}$$

$$R = \frac{\varepsilon}{\varepsilon_\theta}\frac{k_\theta}{k} \tag{31}$$

$$C_{d2} = \left(1.9\left(1 - 0.3\exp\left(-0.0237R_t^2\right)\right) - 1\right) \times (1 - \exp(-0.1754R_\delta))^2 \tag{32}$$

In the above equations, R_δ and R_t are defined in Eqs. (19) and (20) respectively, while the constants appearing in Eq. (8) and in Eqs. (21) – (32) are listed in Table 2. Moreover, $R = \tau_\theta/\tau_u$, defined in Eq. (31), is the ratio between the thermal turbulent characteristic time, $\tau_\theta = k_\theta/\varepsilon_\theta$ and the dynamical turbulent characteristic time, $\tau_u = k/\varepsilon$.

4. Problem description and numerical setup

The present work aims at analyzing the local temperatures on the inner and the outer tube wall as well as the local Nusselt number distribution in a solar tower receiver. Since the latter is composed of many parallel single tubes, only one of them can be taken into account.

4.1. Problem description

The heat flux, and thus the wall temperature, on the tubes of a solar receiver is typically varying along the axis and the circumference, causing high wall thermal stresses when, for example, only one half of the tube's circumference is exposed to the solar irradiation. Therefore, knowledge of the local wall temperatures and convective heat transfer coefficients is very important for a proper design of this crucial component. Another important issue for the design of an asymmetrically heated liquid metal receiver regards the applicability of mean Nusselt number correlations developed for a constant heat flux over the whole surface. The work of [20] for water and of [22] for molten salts have shown that, for these fluids, the available heat transfer correlations for a uniformly heated tube's surface can be sufficiently well applied also to the case with circumferentially non-uniform surface heating. The same analysis has not yet been done for liquid metals heat transfer.

In this work, a representative condition has been analyzed, which mimics the effective boundary conditions a receiver's tube is subjected to. Let us then consider a hydrodynamically turbulent fully developed flow in a tube of length L, with inner radius r_i, outer radius r_o and with thermally insulated end sections, as shown in Fig. 2. Half of the outer wall's surface is heated with a cosinusoidally and longitudinally varying heat flux, expressed as follows:

$$q''_{ow}(\tilde{x}, \varphi) = q''_{ow,max} \cdot \cos\varphi \cdot f(\tilde{x}) \tag{33}$$

In the above equation $\tilde{x} = x/L$ is the non-dimensional axial coordinate, $q''_{ow,max}$ is the maximum heat flux value over the entire outer tube, while the normalized longitudinal heat flux distribution, $f(\tilde{x})$, assumes the following form:

$$f(\tilde{x}) = \exp\left[-\frac{1}{2}\left(\frac{\tilde{x}L - \mu}{\sigma}\right)^2\right] \quad \mu = L/2, \quad \sigma = L/5 \tag{34}$$

Eq. (34) is plotted in Fig. 3 versus the non-dimensional axial distance. It always keeps the same form independently from the length of the tube and the values at both ends are always 5% of the maximum at the center. This flux distribution can be considered as a good approximation of the real one, as shown in Refs. [40,41]. The resulting heat flux on the outer's wall surface is shown in Fig. 4.

4.2. Numerical setup

The turbulence models and their respective boundary conditions described in Sections 3.1 and 3.2 have been implemented through User-Defined-Functions (UDFs) [42] and coupled to the CFD code. Steady-state flow has been assumed and the predictor-corrector *SIMPLE* algorithm [43] has been used for the

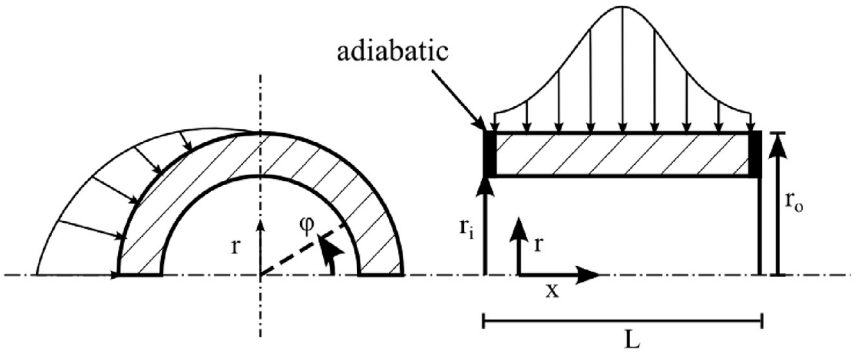

Fig. 2. Schematic representation of the problem and applied boundary conditions.

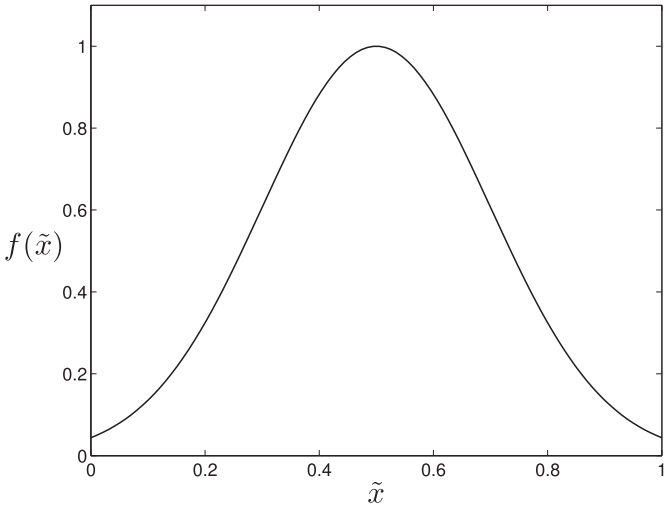

Fig. 3. Normalized longitudinally heat flux distribution along the outer wall of the receiver's tube.

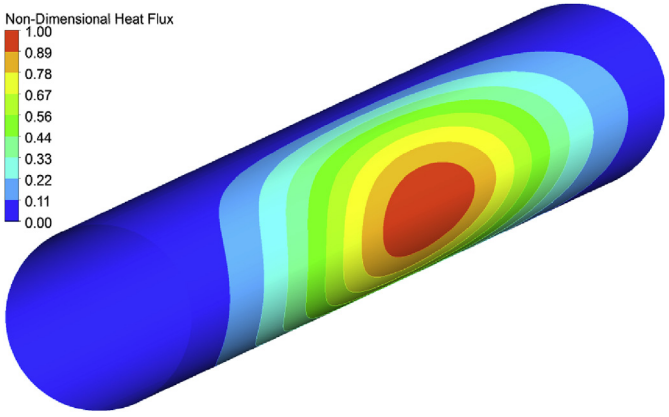

Fig. 4. 3D non-dimensional heat flux distribution on the outer tube's wall.

pressure–velocity coupling. The diffusion terms have been discretized with a central-difference scheme while a second-order upwind scheme is used for the convective terms [44,45]. The gradients at the cell center, necessary for the computation of the scalar values at the cell faces, have been computed with the so-called *least-squares method* [44]. The pressure values at cell faces have been evaluated according to the method of Rhie and Chow [46] and described in Ref. [44]. Buoyancy forces have been neglected and constant thermophysical properties have been considered, resulting in $Pr = 0.025$. This allows to decouple the energy equation from the momentum equations. Therefore, first the latter, together with the turbulence equations of Section 3.1, has been numerically solved. Once a converged solution has been reached, the energy equation, together with the heat turbulence equations of Section 3.2, has been separately solved, keeping the velocity field, k and ε "frozen". The Reynolds number has been varied, resulting in a Péclet number ranging between $1{\cdot}10^3$–$5{\cdot}10^3$, which can be considered as appropriate for liquid metals applications.

In the subsequently described simulations a convergent solution has been assumed when all the following conditions are satisfied: (a) constant average drag coefficient on the walls; (b) constant average convective heat transfer coefficient on the walls; (c) scaled residuals [47] of continuity, momentum and turbulence parameters below 10^{-6}. Due to symmetry reasons, only half of the domain has been simulated. It has been discretized using block-structured non-

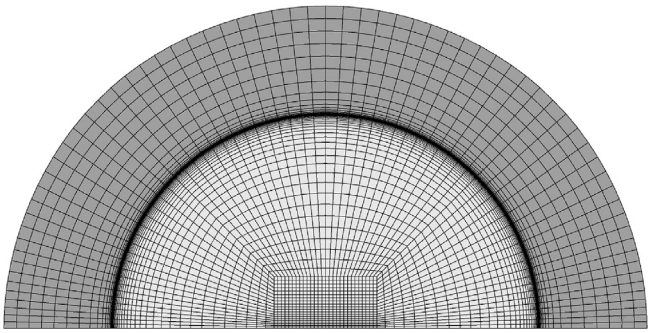

Fig. 5. Hexahedral mesh of a tube's section perpendicular to the flow direction.

Table 3
Discretization errors using the GCI method. The results refer to the simulations of Section 5.3 with $Pe = 2510$, $\lambda^* = 1.4$, $r^* = 1.5$, $L/D = 30$

	$\langle Nu \rangle_L$	C_f
N_1, N_2, N_3	267628, 579908, 1274400	
ϕ_1	21.3128	$4.6720{\cdot}10^{-3}$
ϕ_2	21.2984	$4.6697{\cdot}10^{-3}$
ϕ_3	21.2929	$4.6691{\cdot}10^{-3}$
p	3.53	5.73
ϕ_{ext}^{21}	21.322	$4.669{\cdot}10^{-3}$
e_{ext}^{21}	0.44%	0.011%
GCI_{fine}^{21}	0.055%	0.004%

uniform hexahedral elements, as for example shown in Fig. 5. It must be emphasized that with the mesh used, the solutions for all Re numbers, and thus Pe numbers, considered in the present work have at least two points within a non-dimensional wall distance, y^+, less than one, five points within $y^+ \leq 5$ and ten points within $y^+ \leq 30$, as required by the turbulence model of Section 3 and in order to properly resolve the hydro-dynamical and thermal boundary layers. For the simulations of Section 5.3 the flow has been considered as fully developed and thus cyclic boundary conditions have been imposed for the velocity, k and ε at the inlet and outlet domain's sections [44,48], while for the temperature, k_θ and ε_θ a uniform value has been specified at the inlet section and a zero gradient condition at the outlet. A longitudinally constant mesh

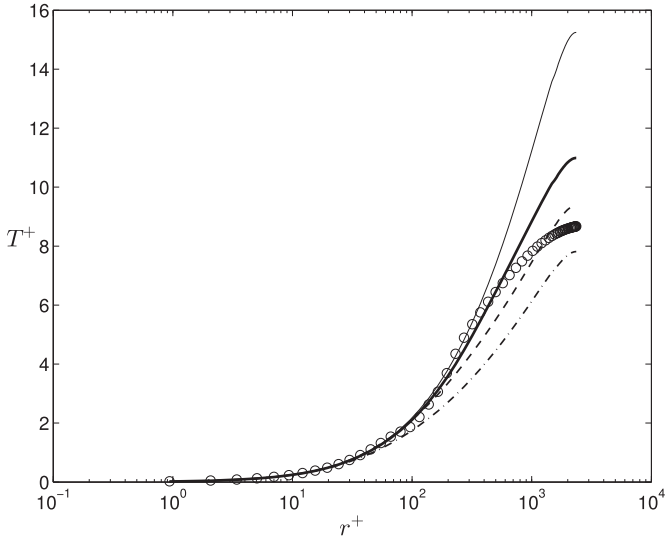

Fig. 6. Non-dimensional mean temperature profiles in a uniformly heated pipe flow at $Re = 10^5$ and $Pr = 0.025$ with $Pr_t = 0.85$ (dot-dashed line), Pr_t from Eq. (35) (dashed line), Pr_t from Eq. (36) (thin solid line), $k-\varepsilon-k_\theta-\varepsilon_\theta$ (thick solid line) and temperature correlation of [53] (○).

Table 4
Percentage error between the Nusselt numbers calculated with Skupinski's correlation [18] and those obtained with the $k-\varepsilon-k_\theta-\varepsilon_\theta$ model and the AKN model together with different Pr_t models.

$k-\varepsilon-k_\theta-\varepsilon_\theta$	Eq. (35), [51]	Eq. (36), [35]	$Pr_t = 0.85$
−3.4%	+13%	−30%	+37%

spacing of $\Delta x^+ = 950$ and $\Delta x^+ = 650$ has been used for the medium and fine grid, respectively, assuring a mesh-independent solution (Table 3). For the simulations of Sections 5.1 and 5.2 both flow and temperature have been considered as being fully developed and thus cyclic boundary conditions have been used for all computed variables. Here, the invariance of the solution along the axial coordinate has allowed to use a much larger axial mesh spacing for the simulations. For all simulations the mass flowrate has been imposed in order to obtain the specified Reynolds number.

The Grid Convergence Index method [49] has been used to quantify the numerical discretization errors. Accordingly, the solution has been computed for three different grids with a refinement ratio of approximately 1.3. Two characteristic variables, namely the circumferentially and longitudinally averaged Nusselt number and the friction factor have been selected as representative for the problem under consideration. The resulting values are summarized in Table 3. The quantity ϕ_i refers to the calculated variable value, while the index $i = 1,2,3$ refers to the fine, medium and coarse grid respectively. The apparent order of the discretization method is denoted by p. The quantities ϕ_{ext}^{21} and e_{ext}^{21} indicate the extrapolated values of the calculated variable from the medium and fine grids and the error, respectively. Both $\langle Nu\rangle_L$ and C_f show monotonic convergence. The numerical uncertainty in the fine-grid solution is given by the GCI_{fine}^{21} values and is therefore very small.

5. Results

5.1. Longitudinally and circumferentially uniform heat flux

The implemented turbulence model has been first validated, for a fully developed turbulent convective flow through a uniformly heated channel and pipe, by comparison with the results obtained by the model's authors [26] and with the DNS data of [31] and [50]. Moreover, simulations at $Re = 10^5$ and $Pr = 0.025$ have been performed for the pipe flow geometry, in order to compare the results

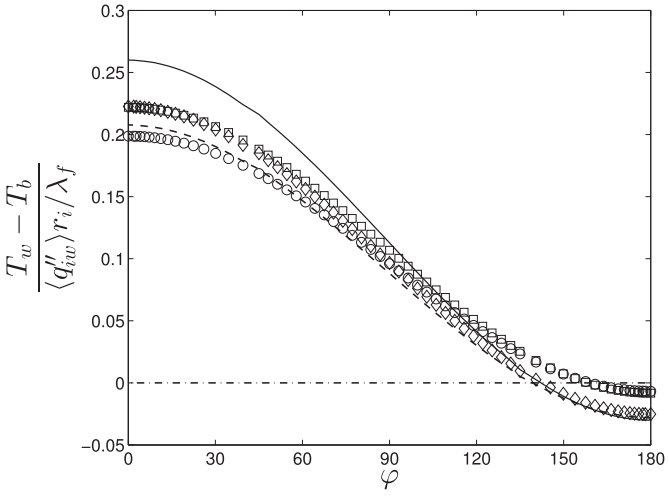

Fig. 7. Comparison between RANS simulations and analytical results for longitudinally constant and cosinusoidal heat flux over the whole tube's circumference at $Re = 10^5$ and $Pr = 0.03$; $k-\varepsilon-k_\theta-\varepsilon_\theta$ model (solid line), "Reynolds" (□),Gärtner et al. [25] (○), AKN with Pr_t from Eq. (35) (◇), AKN with $Pr_t = 0.85$ (dashed line).

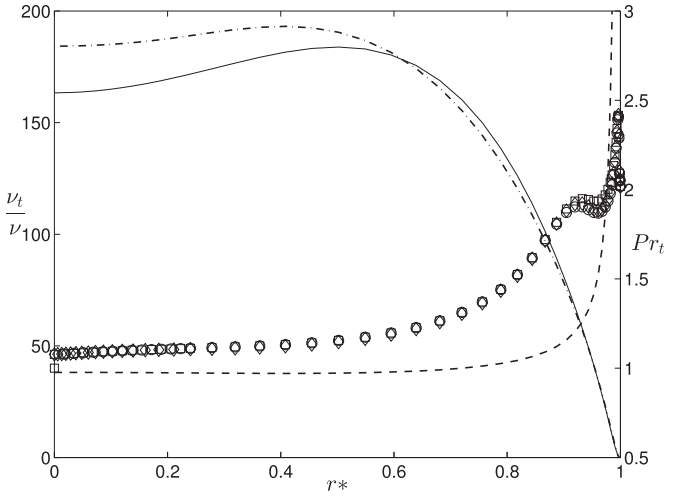

Fig. 8. Models of ν_t/ν and Pr_t compared to RANS simulations; *left y-axis*: ν_t/ν used in Ref. [24] (solid line) and calculated with AKN model (dot-dashed line); *right y-axis*: Pr_t calculated with $k-\varepsilon-k_\theta-\varepsilon_\theta$ model at $\theta = 0°$ (□), $\theta = 90°$ (◇), $\theta = 180°$ (○) and Eq. (35) (dashed line).

obtained using the $k-\varepsilon-k_\theta-\varepsilon_\theta$ model with those achieved by using the AKN model together with the *Reynolds analogy* with $Pr_t = 0.85$ as well as with two correlations for Pr_t:

$$Pr_t = 0.85 + \frac{0.7}{Pr\frac{\nu_t}{\nu}} \tag{35}$$

$$Pr_t = \frac{0.01Pe}{\left[0.018Pe^{0.8} - (7.0 - A)\right]^{1.25}} \tag{36}$$

$$A = \begin{cases} 4.5 & Pe \le 1000 \\ 5.4 - 9\cdot 10^{-4}Pe & 1000 \le Pe \le 2000 \\ 3.6 & Pe \ge 2000 \end{cases}$$

Eq. (35) is an empirical correlation proposed by Kays [51]. It is a fit of the analytical solution for Pr_t by [52] that presumably covers all Prandtl numbers. Eq. (35) only depends on local quantities through ν_t and according to the recent analysis of [37], among three

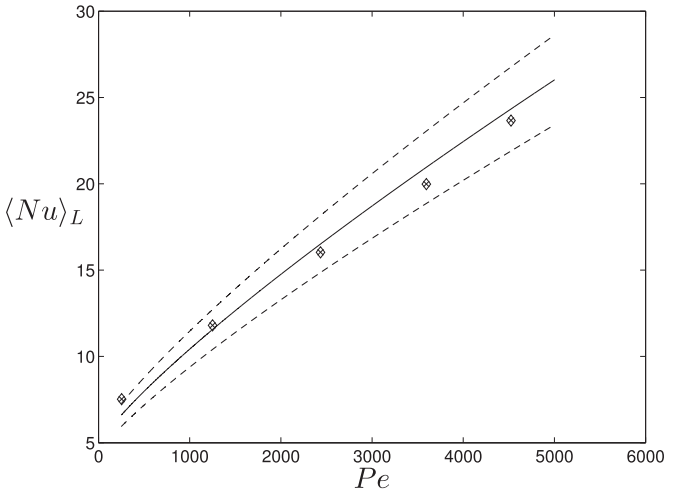

Fig. 9. Nusselt numbers for longitudinally constant heat flux and both uniform heat flux (×) and cosinusoidally varying heat flux over half surface (◇); dashed lines refer to ±10% from the correlation.

Table 5
Governing parameters used for the parametric study.

r^*	λ^*	L/D	Pe
1/1.2/1.5	0.88/1.4/5.5	10/30/50	1255/2510/3766/5021

well established correlations for Pr_t, it shows the best agreement with DNS data of a uniformly heated channel flow. Actually, also a modified version of Eq. (35), where the value 0.7 is substituted with 2.0, is proposed in Ref. [51]. This seems to better fit some available experimental data for liquid metals. However, the same author does not exclude possible consistent experimental errors, also because of the large data scatter for these fluids.

Eq. (36) depends on the global Péclet number and has been proposed by Cheng and Tak [35]. It is based on experimental data and CFD calculations of thermally and hydrodynamically fully developed turbulent convection to fluids with $Pr \approx 0.025$ in tube geometries with constant heat flux.

As can be seen from Fig. 6, the radial temperature profiles for the pipe flow case at $Re = 10^5$, calculated with the above mentioned different approaches for Pr_t, vary significantly. In the same plot also the temperature profile obtained with the correlation of Kader [53] is shown. Best agreement with the latter is achieved with the $k-\varepsilon-k_\theta-\varepsilon_\theta$ model and with the Pr_t model of Eq. (35). Table 4 summarizes the error between the computed Nusselt numbers and the correlation of Skupisnki, which according to [18] has been chosen as the reference one. The $k-\varepsilon-k_\theta-\varepsilon_\theta$ model shows very good agreement with the correlation's value, while none of the results obtained using any of the other Pr_t correlations are within ±10%.

5.2. *Longitudinally constant and circumferentially non uniform heat flux*

The same set of data for the longitudinally and circumferentially uniform heat flux over the whole tube's perimeter are not available for the case of non-uniform applied heat flux. Moreover, although the circular tube is a very common geometry, there is only a limited

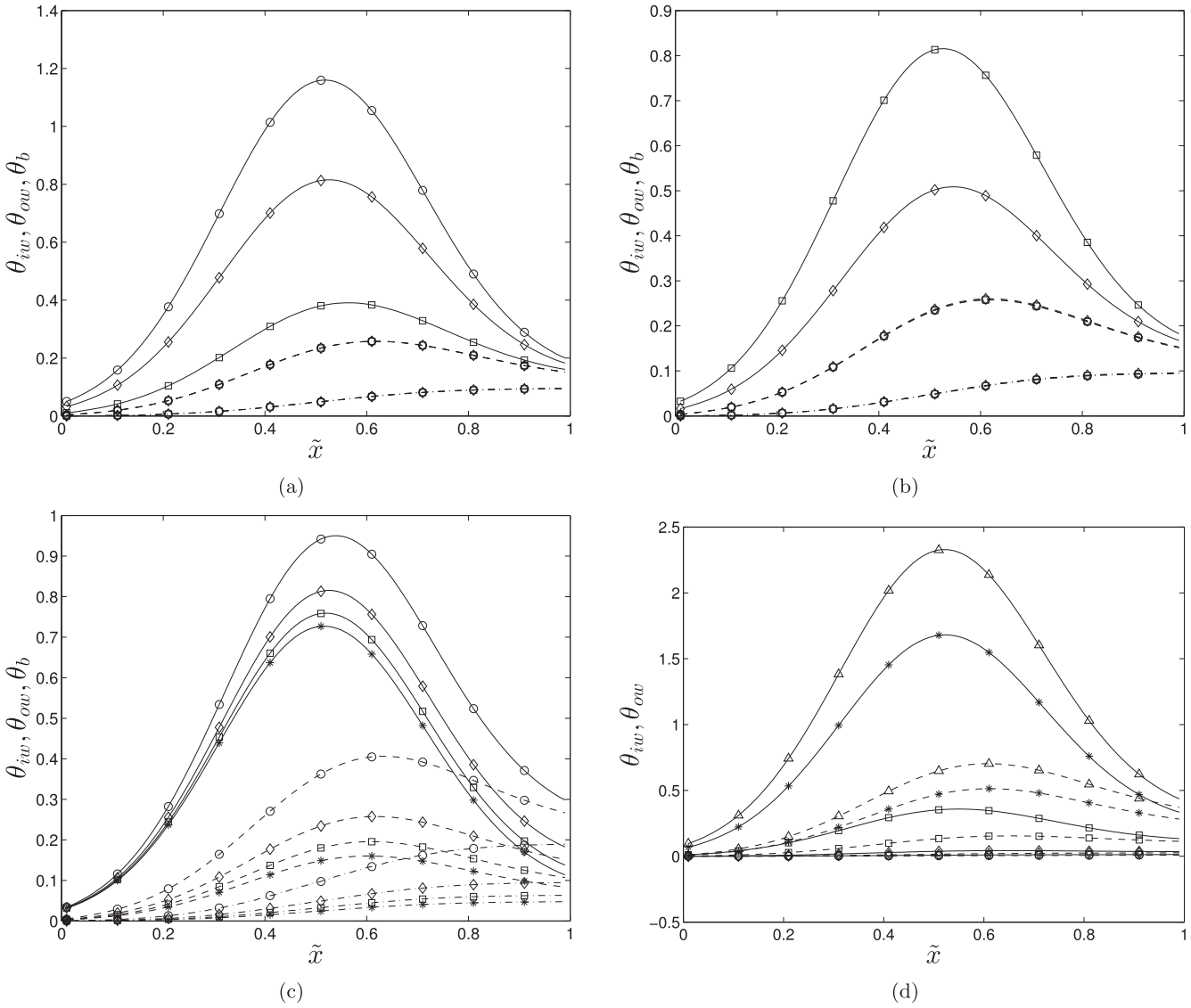

Fig. 10. Profiles of θ_{ow} (solid line), θ_{iw} (dashed line) and θ_b (dashed-dot line) for $L/D = 30$ and *a*)$Pe = 2510$, $r^* = 1.5$; $\lambda^* = 0.88$ (◦), $\lambda^* = 1.4$ (◇), $\lambda^* = 5.5$ (□) *b*)$Pe = 2510$, $\lambda^* = 1.4$; $r^* = 1$ (◦), $r^* = 1.2$ (◇), $r^* = 1.5$ (□) *c*)$r^* = 1.5$, $\lambda^* = 1.4$; $Pe = 1255$ (◦), $Pe = 2510$ (◇), $Pe = 3766$ (□), $Pe = 5021$ (*) *d*)$Pe = 2510$, $r^* = 1.5$, $\lambda^* = 1.4$; $\varphi = 0°$ (◦), $\varphi = 45°$ (◇), $\varphi = 90°$ (□), $\varphi = 135°$ (*), $\varphi = 180°$ (△).

number of experimental investigations for this boundary condition, probably because of the difficulties in the experimental setup. The most comprehensive work the authors are aware of is still the old one of [54] for air. Two others recently appeared for molten salts [22,23] are not as complete in the description of the experimental loop and test conditions as well as in the presented experimental results. Nonetheless, an analytical solution for a longitudinally constant and cosinusoidally varying heat flux distribution over the whole tube's periphery, and in principle valid for all Prandtl numbers, has been first given by Reynolds [24] and successively refined by Gärtner et al. [25]. Therefore, the numerically computed non-dimensional temperature profile obtained with the $k-\varepsilon-k_\theta-\varepsilon_\theta$ turbulence model is compared in Fig. 7 with the analytical results for $Re = 10^5$ and $Pr = 0.03$. A thin wall with negligible thickness and a non-dimensional heat flux of $\tilde{q}''_w = (1+0.5\cos\varphi)$ have been considered in the simulations.

It should be noted that in the paper of Reynolds [24] also for low-Pr number fluids the Nusselt number correlation of Gnielinski [17] has been used to evaluate the wall temperature functions for the mean harmonic. Moreover, the choice of the constant Pr_t used is highly questionable and most likely very inaccurate. Therefore, the results in Fig. 7 denoted as "Reynolds" are the analytical ones we obtained using the same ν_t/ν profile of [24] but using the Nusselt number correlation of Skupinski, as suggested in Refs. [18], together with Pr_t from Eq. (35).

The non-dimensional temperature profile obtained with the present turbulence model differs markedly from that of the above cited references. The differences are more pronounced in the region of higher heat flux, i.e. $0° \le \theta \le 90°$. As shown in Fig. 8, the difference in the radial profile of ν_t/ν adopted by [24] and that resulting from the simulation cannot account for the discrepancy in the values of the non-dimensional temperature profile. Indeed, the results of the simulations with the AKN turbulence model and Pr_t evaluated from Eq. (35) are very close to the "Reynolds"ones. For the sake of completeness, also the simulation results obtained using a constant $Pr_t = 0.85$ are shown and their overall deviation is larger. Therefore, the main source of discrepancy resides in the different values between the turbulent Prandtl number calculated with the $k-\varepsilon-k_\theta-\varepsilon_\theta$ turbulence model from those evaluated with Eq. (35). Their profiles are plotted versus the radial coordinate

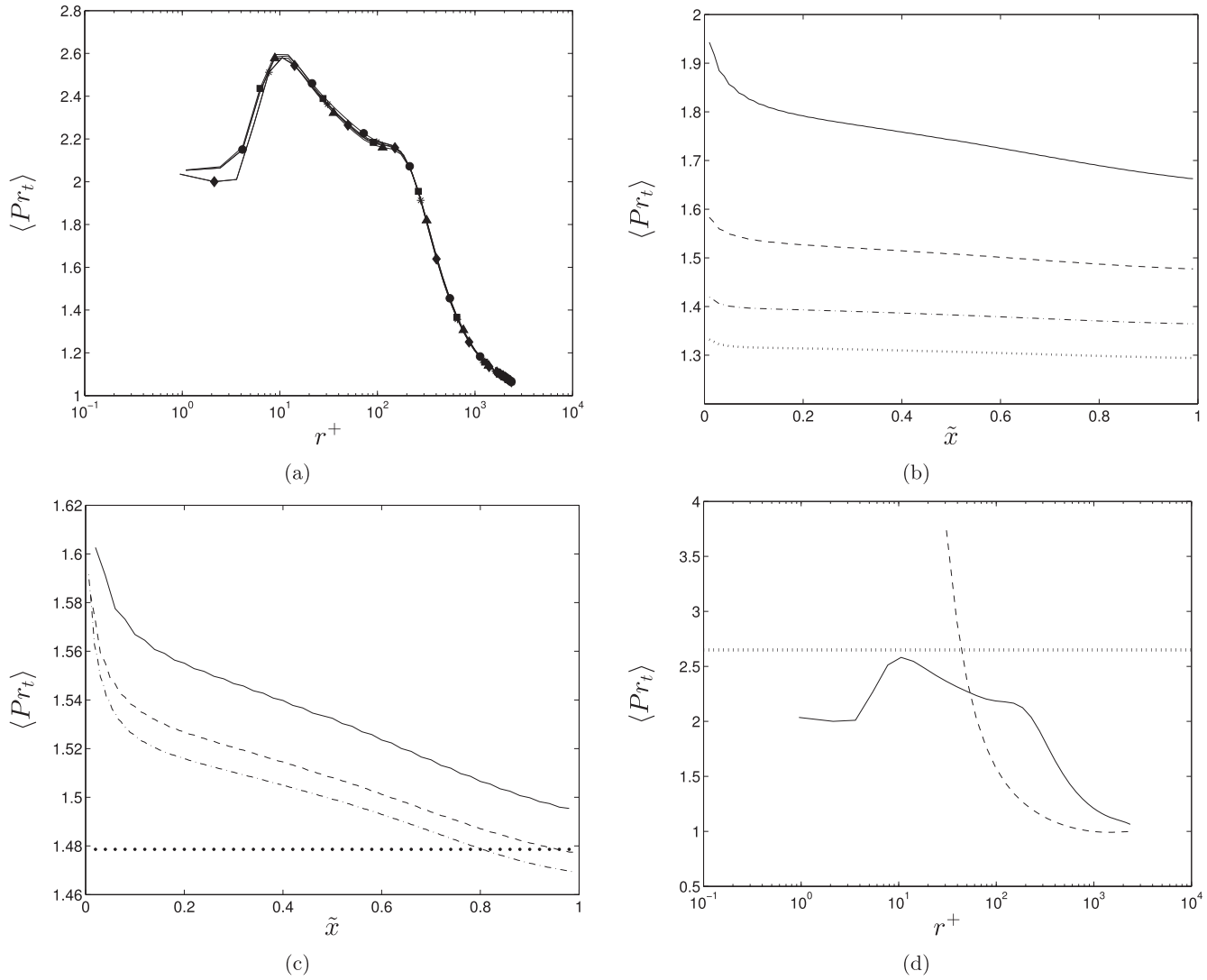

Fig. 11. Profiles of Pr_t for $\lambda^* = 1.4$, $r^* = 1.5$ plotted vs.; *a*)r^+ for $Pe = 2510$, $L/D = 30$, $\bar{x} = 0.5$ and $\varphi = 0°$ (•), $\varphi = 45°$ (◆), $\varphi = 90°$ (■), $\varphi = 135°$ (*), $\varphi = 180°$ (▲) *b*)$\bar{x}$ for $L/D = 30$ and $Pe = 1255$ (solid line), $Pe = 2510$ (dashed line), $Pe = 3766$ (dashed-dot), $Pe = 5021$ (dotted line) *c*)$\bar{x}$ for $Pe = 2510$ and $L/D = 10$ (solid line), $L/D = 30$ (dashed line), $L/D = 50$ (dashed-dot), Pr_t for fully developed flow with longitudinally constant and circumferentially non-uniform heat flux (dotted line) *d*)r^+ for $Pe = 2510$, $L/D = 30$, $\bar{x} = 0.5$ and $k-\varepsilon-k_\theta-\varepsilon_\theta$ (solid line), Kays [51] Eq. (35) (dashed line), Cheng and Tak [35] Eq. (36) (dotted line).

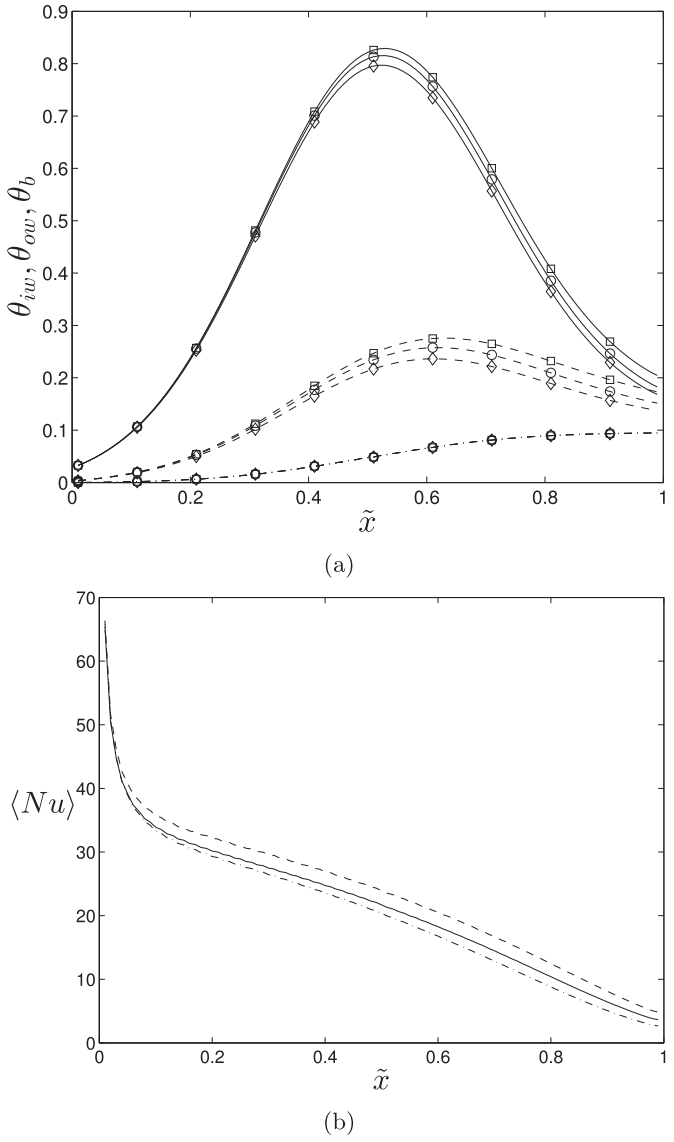

Fig. 12. Comparison of temperature and Nusselt number along $\tilde{x}$ at $\lambda^* = 1.4$, $r^* = 1.5$, $L/D = 30$, $Pe = 2510$ using different approaches to compute Pr_t: *a*)θ_{ow} (solid line), θ_{iw} (dashed line), θ_b (dashed-dot line); $k-\varepsilon-k_\theta-\varepsilon_\theta$ (∘), Kays [51] Eq. (35) (◇),Cheng and Tak [35] Eq. (36) (□) *b*)$k-\varepsilon-k_\theta-\varepsilon_\theta$ (solid line), Kays [51] Eq. (35) (dashed line), Cheng and Tak [35] Eq. (36) (dashed-dot line).

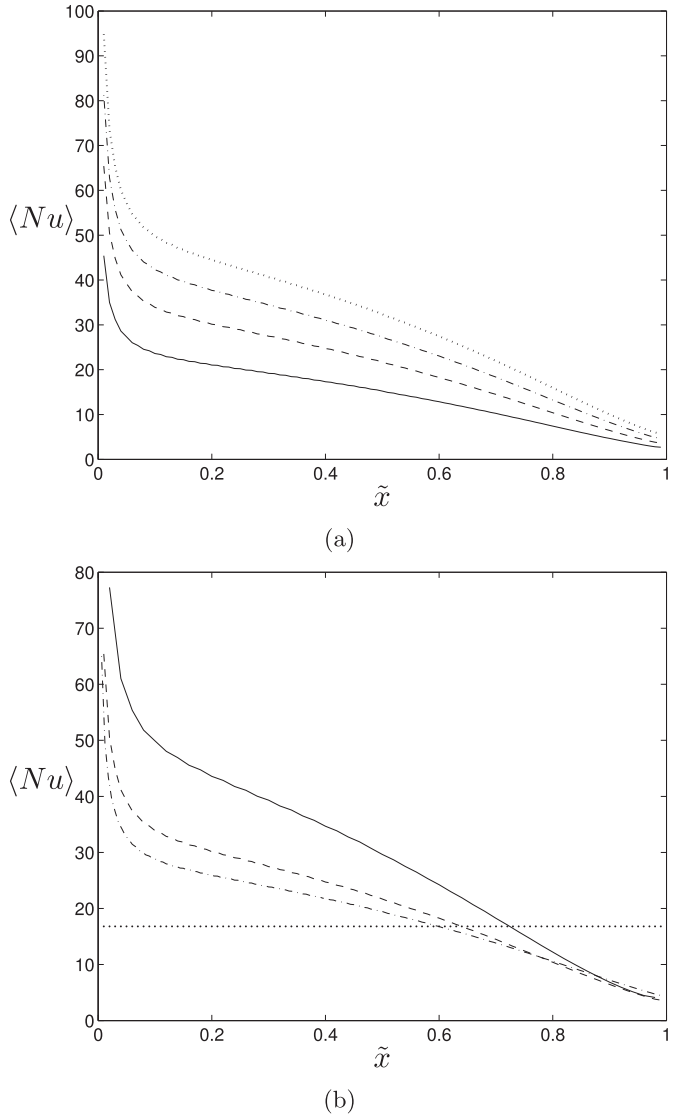

Fig. 13. Profiles of $\langle Nu \rangle$ at $\lambda^* = 1.4$, $r^* = 1.5$ for *a*)$L/D = 30$ and $Pe = 1255$ (solid line), $Pe = 2510$ (dashed line), $Pe = 3766$ (dashed-dot), $Pe = 5021$ (dotted line) *b*)$Pe = 2510$ and $L/D = 10$ (solid line), $L/D = 30$ (dashed line), $L/D = 50$ (dashed-dot line); Nusselt number for fully developed flow evaluated with Skupinski's correlation [18] (dotted line).

in Fig. 8. The values of Pr_t from Eq. (35) tend to infinity when approaching the wall, because ν_t/ν tends to zero. Due to the thicker thermal viscous sublayer of liquid metals compared to medium-to-high Pr number fluids, these high Pr_t values might not be an issue since they imply small values of α_t in a region where molecular conduction effectively dominates. Moreover, even though the profiles of k_θ and ε_θ vary with the radial coordinate for different angular coordinates, φ, the turbulent Prandtl number profiles only show a radial dependency.

The wall temperature predicted with the $k-\varepsilon-k_\theta-\varepsilon_\theta$ model is higher than the other ones in the region of high heat flux, $0^\circ \leq \theta \leq 90^\circ$, and is slightly lower where the non-dimensional temperature assumes negative values, i.e. where the low applied heat flux implies a wall temperature lower than the bulk one. The reason can be found again in the higher predicted Pr_t, as shown in Fig. 8, and therefore in a lower turbulent thermal diffusivity. The latter causes a reduced energy mixing and consequently higher differences between wall and bulk temperatures. Quite surprisingly, the analytical results from Ref. [25] show poor agreement, not only with those obtained with the complete turbulence model of Section 3 but also with the ones evaluated with the AKN model with Pr_t from Eq. (35). The authors used for their calculations a separate expression for the radial and for the tangential turbulent Prandtl number, accounting then also for the anisotropy of the heat flux. Nonetheless, it can be argued that, at least for liquid metal flows, these correlations seem not appropriate.

Fig. 9 shows the circumferentially averaged Nusselt number, defined in Eq. (37), for both a constant and a cosinusoidally varying heat flux over half the wall's perimeter, the other one being adiabatic.

$$\langle Nu \rangle = \frac{\langle q''_{iw} \rangle}{\langle T_w \rangle - T_b} \frac{2r_i}{\lambda_f} \tag{37}$$

The values collapse together at all Péclet numbers and are within a ±10% range from the Skupinski's correlation valid for fully

developed flow with uniform applied surface heat flux. Therefore, as already shown for medium-to-high Prandtl number fluids [20,22], also for liquid metals the Nusselt number correlations for fully developed flow in uniformly heated tubes can be applied to non-uniformly heated cases.

5.3. Longitudinally and circumferentially non-uniform heat flux

From the results of the previous sections it emerges that the $k-\varepsilon-k_\theta-\varepsilon_\theta$ model is appropriate to simulate convective heat transfer to liquid metal flows in tubes. Therefore it has been adopted to study the conjugate turbulent forced convection of a liquid metal flowing in a tube with circumferentially and longitudinally varying heat flux. A parametric study has been done for different combinations of the governing parameters listed in Table 5. According to the authors' experience, these last can be considered as appropriate for engineering problems related to solar thermal receivers.

In Fig. 10a the downstream variation of the dimensionless inner, outer and bulk fluid temperatures, respectively defined in Eqs. (38) – (40), is shown for different solid-to-fluid thermal conductivity ratio, λ^*, while in Fig. 10b the same temperatures are plotted at different outer-to-inner radius ratio, r^*.

$$\theta_{iw}=\frac{(\langle T_{iw}\rangle-T_{b0})\lambda_f}{r_i\left\langle q''_{iw}\right\rangle_L} \tag{38}$$

$$\theta_{ow}=\frac{(\langle T_{ow}\rangle-T_{b0})\lambda_f}{r_i\left\langle q''_{iw}\right\rangle_L} \tag{39}$$

$$\theta_b=\frac{(T_b-T_{b0})\lambda_f}{r_i\left\langle q''_{iw}\right\rangle_L} \tag{40}$$

It can be seen that, at least for the specified range of λ^* and r^* here investigated neither θ_{iw} nor θ_b depend on λ^* or r^*. Indeed, the wall thermal resistance has a damping effect on the heat flux distribution on the inner tube's surface. Conversely, θ_{ow} decreases by decreasing the wall thermal resistance, i.e by an increase of λ^* or a decrease of r^*. The bulk fluid temperature always increases along the length of the duct but not linearly, due to the longitudinally varying heat flux.

The temperatures decrease with increasing Péclet numbers, as shown in Fig. 10c, is more pronounced at low *Pe* and it tends to an asymptotic value with increasing *Pe*.

Finally, Fig. 10d shows the profiles of θ_{iw} and θ_{ow} along the tube's axis at different angular positions. Note that in this case the local values of T_{iw} and T_{ow} are used instead of the circumferentially averaged ones of Eqs. (38) and (39). The maximum temperature values can be seen for $\varphi=180^\circ$, i.e. where also the heat flux has its peak value, as shown in Fig. 2. Due to the decrease of the longitudinal applied heat flux, the temperatures also decrease starting from a certain axial position, with the exception of the profiles at $\varphi=0^\circ$ and $\varphi=45^\circ$. Here, where the outer wall is adiabatic, the temperatures always slightly increase due to the circumferential conduction in the wall and in the fluid.

From Fig. 11a, which shows the profiles of Pr_t at different angular coordinates on a section along the tube's axis, it can be noted how the values calculated with the $k-\varepsilon-k_\theta-\varepsilon_\theta$ model are almost independent from the angular position.

Fig. 11b shows the variation of the cross-section averaged Pr_t along the axial coordinate at different Péclet numbers. As expected, Pr_t decreases with increasing *Pe* because of the increased turbulent mixing. Moreover, except for the lowest value of *Pe*, Pr_t almost attains a constant value over the tube's length and seems to tend to a common value with increasing *Pe*.

Fig. 11c illustrates the profiles of the circumferentially averaged Pr_t versus the axial coordinate for different length-over-diameter ratios. The values decrease with increasing *L*/*D*. The decrease is more accentuated for low *L*/*D*. The values remain always higher than those for the fully developed case, i.e. for a longitudinally constant heat flux, except close to the outlet section, where, for high *L*/*D* ratios, they can go slightly beyond the fully developed ones.

Fig. 11d shows a comparison between the calculated values of Pr_t using the $k-\varepsilon-k_\theta-\varepsilon_\theta$ model and Eqs. (35) and (36). The correlation of Eq. (36) strongly overestimates the value of the turbulent Prandtl number with respect to the other two.

As shown in sub Fig. 12a and b respectively, the temperature profiles and the circumferentially averaged Nusselt numbers calculated with the different approaches for Pr_t are quite similar, while in the case of fully developed flow they were markedly

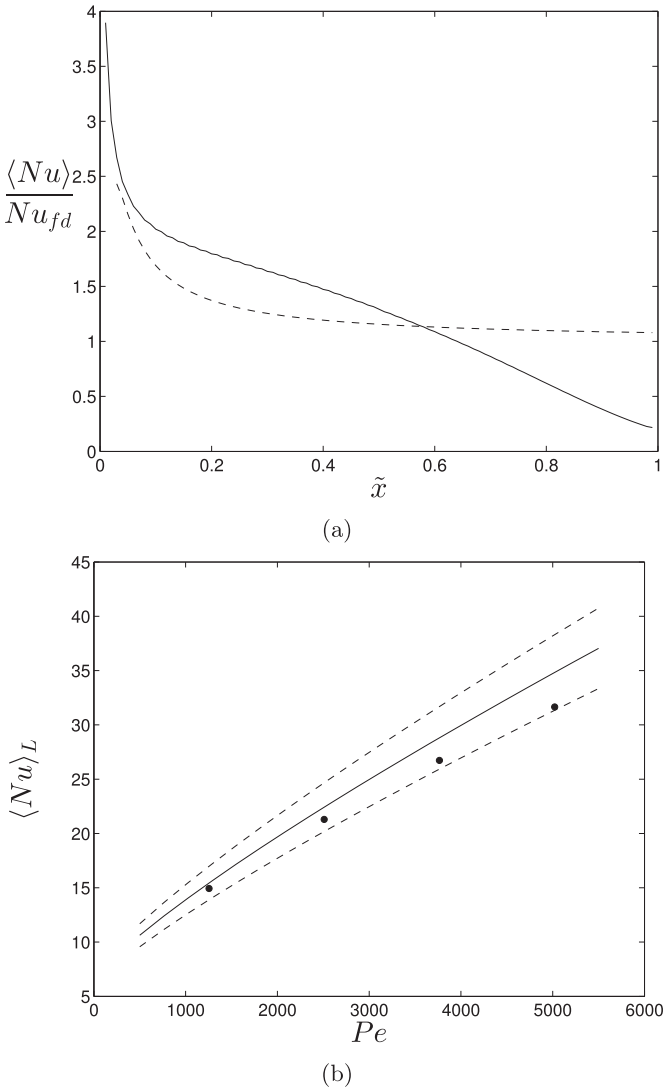

Fig. 14. *a)* Axial profiles of Nusselt number for $\lambda^*=1.4$, $r^*=1.5$, $L/D=30$ evaluated with the $k-\varepsilon-k_\theta-\varepsilon_\theta$ model (solid line) and with the correlation of Ching-Jen and Chiou [56], Eq. (41) (dashed line) using Skupinski's correlation for Nu_{fd}*b)* Longitudinally and circumferentially averaged Nusselt number evaluated with the $k-\varepsilon-k_\theta-\varepsilon_\theta$ model at different Péclet numbers (●); Ching-Jen and Chiou [56], Eq. (42) using Skupinski's correlation for Nu_{fd} (solid line); dashed lines refer to a deviation of ±10% from the previous correlation.

different. The reason is the developing thermal boundary layer in the case of longitudinally varying heat flux and therefore the higher temperature gradients with respect to the fully developed case. These compensate the differences in the turbulent Prandtl number, shown in Fig. 11d, and thus in the turbulent thermal diffusivity, enhancing then the energy mixing.

As shown in Fig. 13, the Nusselt number increases with increasing *Pe* because of the enhanced turbulence intensity. Conversely, it decreases with increasing *L*/*D* for the same *Pe* number because of the lower temperature gradients at the same $\tilde{x}$ due to the increased developing length. This effect is more accentuated at low *L*/*D*, while the curves tend to collapse together at higher length-to-diameter ratios. It should also be noted that, due to the shape of the applied heat flux, the *Nu* numbers can become also lower than those for fully developed flow, as already found for example by [55] for a sinusoidally heat flux distribution along a cylindrical fuel element.

The circumferentially averaged and global Nusselt number values, these last calculated at different Péclet numbers, have been compared in Fig. 14 with the predicted ones using the following correlations proposed in Ref. [56] for the local, Eq. (41), and the mean Nusselt number, Eq. (42), respectively:

$$\frac{\langle Nu\rangle}{Nu_{fd}} = 1 + \frac{2.4}{x/2r_i} - \frac{1}{(x/2r_i)^2} \tag{41}$$

$$\frac{\langle Nu\rangle_L}{Nu_{fd}} = 1 + \frac{7.0}{x/2r_i} + \frac{2.8}{x/2r_i}\ln\left(\frac{x/2r_i}{10}\right) \tag{42}$$

The above equations hold for a uniformly heated duct at $Pr < 0.03$, $Pe > 500$ and $x/2r_i > 2$. The fully developed Nusselt number, Nu_{fd}, has been evaluated with the correlation of Skupinski [18] instead of using the one proposed by [56]. As shown in Fig. 14a, even though the local Nu values differ substantially from those evaluated with Eq. (41), the global ones in Fig. 14b are within the range of ±10% of the correlation. This is only due to the averaging procedure that flattens the local differences. Moreover, the error between the computed values of $\langle Nu\rangle$ and $\langle Nu\rangle_L$ and those from Eqs. (41) and (42), respectively, increases with increasing *Pe* number and also with increasing *L*/*D* ratio.

Finally, Fig. 15 shows the non-dimensional radial heat flux for $Pe = 2510$ at three different axial positions and at two circumferential angles, namely at the maximum local heat flux, $\varphi = 0°$, and at $\varphi = 45°$. The peak values shift to higher r^+ with increasing $\tilde{x}$ and their magnitude also raises because of the higher temperature gradients away from the wall. It can be also noted that the profiles at different angles collapse at the same axial position. Both the shape and the magnitude of $\overline{u_r' T'}^+$ are similar to those for a uniformly heated surface.

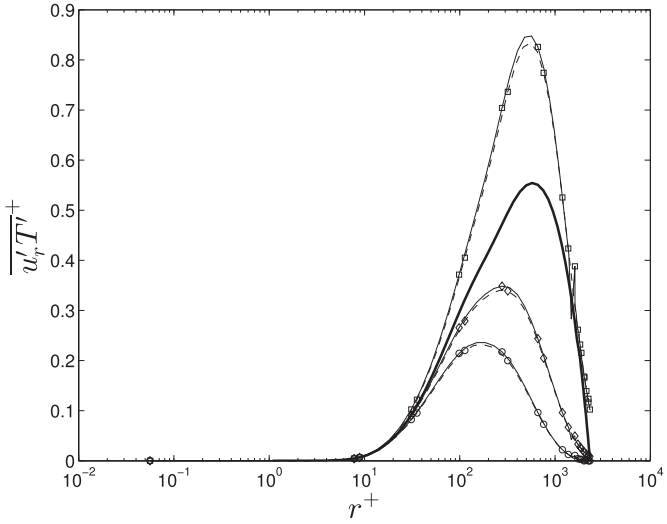

Fig. 15. Non-dimensional radial turbulent heat flux $\overline{u_r' T'}^+$ vs. r^+ for $Pe = 2510$ at $\tilde{x} = 0.25$ (∘), $\tilde{x} = 0.5$ (◇), $\tilde{x} = 0.75$ (□) and $\varphi = 0°$ (solid line), $\varphi = 45°$ (dashed-dot line). The values for the uniformly heated surface are also shown (thick solid line).

6. Conclusions

The conjugate heat transfer in the receiver tube of a solar thermal tower operated with a liquid metal having a representative Prandtl number of 0.025 has been numerically analyzed. A circumferentially and longitudinally non-uniform heat flux has been applied on half the outer wall surface, while the other half has been considered as adiabatic. According to the author's knowledge, there are presently no investigations for liquid metal flows subjected to these boundary conditions. This analysis has been motivated by the recently renewed interest in using liquid metals as heat transfer fluids for CSP applications.

Since the Reynolds analogy, that assumes a constant turbulent Prandtl number close to unity, does not apply to liquid metals, a four-equations $k-\varepsilon-k_\theta-\varepsilon_\theta$ eddy-viscosity turbulence models has been used. Besides the equations for the turbulent kinetic energy and its dissipation rate, two additional ones, namely for the temperature variance and its dissipation rate, have been solved, in order to locally calculate the turbulent thermal diffusivity. For the turbulent convection in a pipe with uniformly distributed heat flux on the wall, this model has shown to better perform compared to the results obtained using correlations especially developed to compute Pr_t in liquid metal flows.

Simulations with the $k-\varepsilon-k_\theta-\varepsilon_\theta$ model, and also using correlations for Pr_t, have been performed for the case of a longitudinally uniform and circumferentially cosinusoidal heat flux. The $k-\varepsilon-k_\theta-\varepsilon_\theta$ model shows markedly different results compared to available semi-analytical solutions and those obtained using the above cited correlations. This is attributed to the differences in the computed Pr_t. Nonetheless, the values of the circumferentially averaged Nusselt number agree with those for a uniformly distributed heat flux and are within a ±10% range from a Nusselt number correlation valid for fully developed flow with uniform applied surface heat flux. Therefore, as already shown in literature for medium-to-high Prandtl number fluids, also for liquid metals Nusselt number correlations for fully developed flow in uniformly heated tubes can be applied to non-uniformly heated cases. However, it must be emphasized that these correlations are not suited to evaluate the local wall temperatures and Nusselt numbers, that indeed have a quite uneven circumferential profile.

The conjugate heat transfer for a longitudinally and circumferentially varying heat flux has been analyzed for different values of the governing parameters, i.e. the solid-to-fluid thermal conductivity, the wall thickness ratio, the Péclet number and the diameter-to-length ratio. The values have been chosen such as to be appropriate for engineering applications. Detailed results for the inner, outer, fluid bulk temperature, Pr_t and Nusselt number have been reported. Contrarily to the case of thermally fully developed flow, the temperature profiles and the circumferentially averaged Nusselt numbers calculated both with the $k-\varepsilon-k_\theta-\varepsilon_\theta$ model and the correlations for Pr_t are quite similar. The reason lies in the developing thermal boundary layer and consequently in the higher temperature gradients that dampen the differences in Pr_t and enhance the energy mixing. The circumferentially averaged Nusselt numbers along the tube's axis and the circumferentially and longitudinally averaged ones have been compared to those obtained with a correlation valid for fully developed flow within a uniformly heated pipe. Although the first differ substantially from the correlation's ones, the second are within a ±10% range. This is, however, only due to the averaging procedure that cancels out the

local differences. The values of the non-dimensional radial turbulent heat flux increase along the tube's axis but its shape and magnitude are similar to those for a uniformly heated surface.

Acknowledgements

The authors wish to acknowledge the support of the Helmholtz Association in the framework of the Helmholtz-Alliance LIMTECH (Liquid Metal Technology), Subtopic B2: Liquid Metals for Solar Power Systems.

References

[1] P.E. Kesselring (Ed.), The IEA/SSPS Solar Thermal Power Plants - Facts and Figures - Final Report of the International Test and Evaluation Team (ITET), vol. 1, Springer, Berlin, 1986.
[2] W.J. Schiel, M.A. Geyer, Testing an external sodium receiver up to heat fluxes of 2.5 MW/m^2: results and conclusions from the IEA-SSPS high flux experiment conducted at the central receiver system of the Plataforma Solar de Almeria (Spain), Sol. Energy 41 (1988) 255–265.
[3] J. Pacio, C. Singer, T. Wetzel, R. Uhlig, Thermodynamic evaluation of liquid metals as heat transfer fluids in concentrated solar power plants, Appl. Therm. Eng. 60 (2013) 295–302.
[4] D. Frazer, E. Stergar, C. Cionea, P. Hosemann, Liquid metal as a heat transport fluid for thermal solar power applications, Energy Procedia 49 (2014) 627–636. Proceedings of the SolarPACES 2013 International Conference.
[5] J.P. Kotzé, T.W. von Backström, P.J. Erens, NaK as a primary heat transfer fluid in thermal solar power installations, in: Proceedings of the SolarPACES 2012 International Conference, 2012.
[6] N. Boerema, G. Morrison, R. Taylor, G. Rosengarten, Liquid sodium versus Hitec as a heat transfer fluid in solar thermal central receiver systems, Sol. Energy (2012) 2293–2305.
[7] C. Singer, R. Buck, R. Pitz-Paal, H. Müller-Steinhagen, Economic potential of innovative receiver concepts with different solar field configurations for supercritical steam cycles, J. Sol. Energy Eng., Trans. ASME 136 (2013). Article number 021009.
[8] J. Pacio, T. Wetzel, Assessment of liquid metal technology status and research paths for their use as efficient heat transfer fluids in solar central receiver systems, Sol. Energy 93 (2013) 11–22.
[9] J. Pacio, A. Fritsch, C. Singer, R. Uhlig, Liquid metals as efficient coolants for high-intensity point-focus receivers: implications to the design and performance of next-generation CSP systems, Energy Procedia 49 (2014) 647–655. Proceedings of the SolarPACES 2013 International Conference.
[10] T. Wetzel, J. Pacio, L. Marocco, A. Weisenburger, A. Heinzel, W. Hering, C. Schroer, G. Müller, J. Konys, R. Stieglitz, J. Fuchs, J. Knebel, C. Fazio, M. Daubner, F. Fellmoser, Liquid metal technology for concentrated solar power systems: contributions by the german research program, AIMS Energy 2 (2014) 89–98.
[11] J. Flesch, A. Fritsch, G. Cammi, L. Marocco, F. Fellmoser, J. Pacio, T. Wetzel, Construction of a test facility for demonstration of a liquid lead-bismuth-cooled 10 kW thermal receiver in a solar furnace arrangement - {SOMMER}, Energy Procedia 69 (2015) 1259–1268. International Conference on Concentrating Solar Power and Chemical Energy Systems, SolarPACES 2014.
[12] Lundy Sargent, Assessment of Parabolic Trough and Power Tower Solar Technology Cost and Performance Forecasts, Technical Report, Sargent & Lundy LLC Consulting Group, National Renewable Energy Laboratory, Chicago, Illinois; Golden, Colorado (US), 2003.
[13] J. García-Barberena, A. Monreal, A. Mutuberria, M. Snchez, Towards cost-competitive solar towers energy cost reductions based on decoupled solar combined cycles (DSCC), Energy Procedia 49 (2014) 1350–1360. Proceedings of the SolarPACES 2013 International Conference.
[14] R. Pitz-Paal, Dersch B. Milow, ECOSTAR European Concentrated Solar Thermal Road-mapping, Technical Report, German Aerospace Center (DLR), 2003.
[15] R. Stieglitz, Low Prandtl number thermal hydraulics, in: Handbook on Lead-bismuth Eutectic Alloy and Lead Properties, Materials Compatibility, Thermal-hydraulics and Technologies, OECD/NEA Nuclear Science Committee, 2007.
[16] W. Kays, M. Crawford, B. Weigand, Convective Heat and Mass Transfer, fourth ed., McGraw-Hill, 2005.
[17] M. Bhatti, R. Shah, Turbulent and transition flow convective heat transfer, in: S. Kakaç, R.K. Shah, W. Aung (Eds.), Handbook of Single-phase Convective Heat Transfer, John Wiley & Sons, Inc, 1987.
[18] J. Pacio, L. Marocco, T. Wetzel, Review of data and correlations for turbulent forced convective heat transfer of liquid metals in pipes, Heat Mass Transf. 51 (2014) 153–164.
[19] M. Roldán, L. Valenzuela, E. Zarza, Thermal analysis of solar receiver pipes with superheated steam, Appl. Energy 103 (2013) 73–84.
[20] I.F. Okafor, J. Dirker, J.P. Meyer, Influence of circumferential solar heat flux distribution on the heat transfer coefficients of linear fresnel collector absorber tubes, Sol. Energy 107 (2014) 381–397.
[21] D.H. Lobón, E. Baglietto, L. Valenzuela, E. Zarza, Modeling direct steam generation in solar collectors with multiphase CFD, Appl. Energy 113 (2014) 1338–1348.
[22] X. Yang, X. Yang, J. Ding, Y. Shao, H. Fan, Numerical simulation study on the heat transfer characteristics of the tube receiver of the solar thermal power tower, Appl. Energy 90 (2012) 142–147. Energy Solutions for a Sustainable World, Special Issue of International Conference of Applied Energy, ICA2010, April 21-23, 2010, Singapore.
[23] C. Chang, X. Li, Q. Zhang, Experimental and numerical study of the heat transfer characteristics in solar thermal absorber tubes with circumferentially non-uniform heat flux, Energy Procedia 49 (2014) 305–313. Proceedings of the SolarPACES 2013 International Conference.
[24] W. Reynolds, Turbulent heat transfer in a circular tube with variable circumferential heat flux, Int. J. Heat Mass Transf. 6 (1963) 445–454.
[25] D. Gärtner, K. Johannsen, H. Ramm, Turbulent heat transfer in a circular tube with circumferentially varying thermal boundary conditions, Int. J. Heat Mass Transf. 17 (1974) 1003–1018.
[26] S. Manservisi, F. Menghini, A CFD four parameter heat transfer turbulence model for engineering applications in heavy liquid metals, Int. J. Heat Mass Transf. 69 (2014) 312–326.
[27] A. Shams, F. Roelofs, E. Baglietto, S. Lardeau, S. Kenjeres, Assessment and calibration of an algebraic turbulent heat flux model for low-prandtl fluids, Int. J. Heat Mass Transf. 79 (2014) 589–601.
[28] S. Kenjereš, K. Hanjalić, Convective rolls and heat transfer in finite-length Rayleigh-Bénard convection: a two-dimensional numerical study, Phys. Rev. E 62 (2000) 7987–7998.
[29] S. Kenjereš, K. Hanjalić, LES, T-RANS and hybrid simulations of thermal convection at high Ra numbers, Int. J. Heat Fluid Flow 27 (2006) 800–810. Special Issue of the 6th International Symposium on Engineering Turbulence Modelling and Measurements {ETMM6}.
[30] H. Kawamura, K. Ohsaka, H. Abe, K. Yamamoto, DNS of turbulent heat transfer in channel flow with low to medium-high Prandtl number fluid, Int. J. Heat Fluid Flow 19 (1998) 482–491.
[31] H. Kawamura, H. Abe, Y. Matsuo, DNS of turbulent heat transfer in channel flow with respect to Reynolds and Prandtl number effects, Int. J. Heat Fluid Flow 20 (1999) 196–207.
[32] H. Abe, H. Kawamura, Y. Matsuo, Surface heat-flux fluctuations in a turbulent channel flow up to Re_τ=1020 with Pr=0.025 and 0.71, Int. J. Heat Fluid Flow 25 (2004) 404–419. Turbulence and Shear Flow Phenomena (TSFP-3).
[33] I. Tiselj, DNS of turbulent channel flow at Re_τ=395, 590 and Pr=0.01, in: The 14th International Topical Meeting on Nuclear Reactor Thermalhydraulics (NURETH-14), 2014.
[34] X. Cheng, N. Tak, CFD analysis of thermalhydraulic behavior of heavy liquid metals in sub-channels, Nucl. Eng. Des. 236 (2006) 1874–1885.
[35] X. Cheng, N. Tak, Investigation on turbulent heat transfer to lead – bismuth eutectic flows in circular tubes for nuclear applications, Nucl. Eng. Des. 236 (2006) 385–393.
[36] S. Manservisi, F. Menghini, Triangular rod bundle simulations of a CFD $k-\varepsilon-k_\theta-\varepsilon_\theta$ heat transfer turbulence model for heavy liquid metals, Nucl. Eng. Des. 273 (2014) 251–270.
[37] M. Duponcheel, L. Bricteux, M. Manconi, G. Winckelmans, Y. Bartosiewicz, Assessment of RANS and improved near-wall modeling for forced convection at low prandtl numbers based on LES up to Re_τ=2000, Int. J. Heat Mass Transf. 75 (2014) 470–482.
[38] G. Grötzbach, Challenges in low-Prandtl number heat transfer simulation and modelling, Nucl. Eng. Des. 264 (2013) 41–55.
[39] K. Abe, T. Kondoh, Y. Nagano, A new turbulence model for predicting fluid flow and heat transfer in separating and reattaching flows – I. Flow field calculations, Int. J. Heat Mass Transf. 37 (1994) 139–151.
[40] F. Collado, A. Gómez, J. Turégano, An analytic function for the flux density due to sunlight reflected from a heliostat, Sol. Energy 37 (1986) 215–234.
[41] A. Sánchez-González, D. Santana, Solar flux distribution on central receivers: a projection method from analytic function, Renew. Energy 74 (2015) 576–587.
[42] Ansys Inc, Fluent UDF Manual v.15, 2014.
[43] J. Ferziger, M. Perić, Computational Methods for Fluid Dynamics, third ed., Springer, Berlin Heidelberg, 2001.
[44] Ansys Inc, Fluent Theory Guide v.15, 2014.
[45] T. Barth, D. Jespersen, The Design and Application of Upwind Schemes on Unstructured Meshes, Technical report AIAA PAPER 89–0366, NASA Ames Research Center, Moffett Field, CA, United States, 1989.
[46] C. Rhie, W. Chow, A Numerical Study of the Turbulent Flow Past an Isolated Airfoil with Trailing Edge Separation, Technical report AIAA PAPER 82–0998, NASA Ames Research Center, Moffett Field, CA, United States, 1982.
[47] Ansys Inc, Fluent User Guide v.15, 2014.
[48] S. Patankar, C. Liu, E. Sparrow, The periodic thermally developed regime in ducts with streamwise periodic wall temperature or heat flux, Int. J. Heat Mass Transf. 21 (1978) 557–566.
[49] I. Celik, U. Ghia, P. Roache, C. Freitas, H. Coleman, P. Raad, Procedure for estimation and reporting of uncertainty due to discretization in CFD applications, ASME J. Fluids Eng. 130 (7) (2008).
[50] S. Saha, C. Chin, H. Blackburn, A. Ooi, The influence of pipe length on thermal statistics computed from DNS of turbulent heat transfer, Int. J. Heat Fluid Flow 32 (2011) 1083–1097.
[51] W. Kays, Turbulent Prandtl number - where are we? J. Heat. Transf. 116 (1994) 284–295.
[52] V. Yakhot, S.A. Orszag, A. Yakhot, Heat transfer in turbulent fluids – I. Pipe flow, Int. J. Heat Mass Transf. 30 (1987) 15–22.

[53] B. Kader, Temperature and concentration profiles in fully turbulent boundary layers, Int. J. Heat Mass Transf. 24 (1981) 1541–1544.
[54] A. Black, E. Sparrow, Experiments on turbulent heat transfer in a tube with circumferentially varying thermal boundary conditions, J. Heat. Transf. 89 (1967) 258–268.
[55] W. Hall, P. Price, The effect of a longitudinally varying heat flux on the heat transfer coefficient for turbulent flow in a pipe, in: International Heat Transfer Conference, ASME IMechE, Boulder, Co, 1961.
[56] C. Ching-Jen, J.S. Chiou, Laminar and turbulent heat transfer in the pipe entrance region for liquid metals, Int. J. Heat Mass Transf. 24 (1981) 1179–1189.